

# Data-Driven Sub-Riemannian Geodesics in $SE(2)$

E.J. Bekkers<sup>2</sup>, R. Duits<sup>1,2</sup>(✉), A. Mashtakov<sup>2</sup>, and G.R. Sanguinetti<sup>1</sup>(✉)

<sup>1</sup> Department of Mathematics and Computer Science,  
Eindhoven University of Technology, Eindhoven, The Netherlands  
G.R.Sanguinetti@tue.nl

<sup>2</sup> Department of Biomedical Engineering,  
Eindhoven University of Technology, Eindhoven, The Netherlands  
{E.J.Bekkers,R.Duits,A.Mashtakov,G.R.Sanguinetti}@tue.nl

**Abstract.** We present a new flexible wavefront propagation algorithm for the boundary value problem for sub-Riemannian (SR) geodesics in the roto-translation group  $SE(2) = \mathbb{R}^2 \rtimes S^1$  with a metric tensor depending on a smooth external cost  $\mathcal{C} : SE(2) \rightarrow [\delta, 1]$ ,  $\delta > 0$ , computed from image data. The method consists of a first step where geodesically equidistant surfaces are computed as a viscosity solution of a Hamilton-Jacobi-Bellman (HJB) system derived via Pontryagin's Maximum Principle (PMP). Subsequent backward integration, again relying on PMP, gives the SR-geodesics. We show that our method produces geodesically equidistant surfaces. For  $\mathcal{C} = 1$  we show that our method produces the global minimizers, and comparison with exact solutions shows a remarkable accuracy of the SR-spheres/geodesics. Finally, trackings in synthetic and retinal images show the potential of including the SR-geometry.

**Keywords:** Roto-translation group · Hamilton-Jacobi equations · Vessel tracking · Sub-riemannian geometry · Morphological scale spaces

## 1 Introduction

In computer vision, a strategy to address the problem of salient curve extraction is the notion of geodesics or minimal paths where some cost function is considered over the image domain such that it has a low value on locations with high curve saliency. The minimizing geodesic is defined as the curve that minimizes the length of the curve weighted by the cost function. To compute data-adaptive geodesics many authors use a two step approach in which firstly a geodesic distance map to a source is computed and then steepest descent on the map

---

E.J. Bekkers, R. Duits, A. Mashtakov and G.R. Sanguinetti— Joint main Authors.  
The research leading to the results of this article has received funding from the European Research Council under the ECs 7th Framework Programme (FP7/2007 2014)/ERC grant agreement No. 335555 and from (FP7-PEOPLE-2013-ITN)/EU Marie-Curie ag. no. 607643.

gives the geodesics. In a PDE framework, the geodesic map can be obtained via wavefront propagation as the viscosity solution of a Hamilton-Jacobi equation. For a review of this approach and applications see [22, 26, 28].

Another set of geodesic methods, partially inspired by the psychology of vision was developed in [11, 25]. Here, the roto-translation group  $SE(2) = \mathbb{R}^2 \rtimes S^1$  endowed with a sub-Riemannian (SR) metric models the functional architecture of the primary visual cortex and geodesics are used for completion of occluded contours. A stable wavelet-like approach to lift 2D-images to functions on  $SE(2)$  was proposed in [12]. Within the  $SE(2)$  framework, images and curves are lifted to the 3D space  $\mathbb{R}^2 \rtimes S^1$  of coupled positions and orientations in which intersecting curves are disentangled. The SR-structure applies a restriction to so-called horizontal curves which are the curves naturally lifted from the plane (see Fig. 1A). For explicit formulas of SR-geodesics and optimal synthesis see [27]. SR-geodesics in  $SE(2)$  were also studied in [6, 7, 14, 18, 20]. Here, we propose a

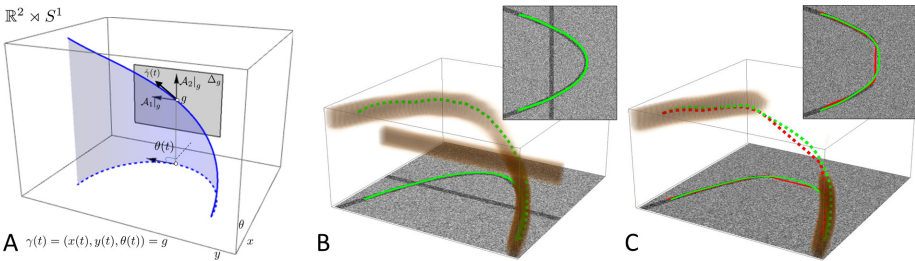


**Fig. 1.** **A:** Every point in the planar curve  $\gamma_{2D}(t) = (x(t), y(t))$  is lifted to a point  $g = \gamma(t) = (x(t), y(t), \theta(t)) \in SE(2)$  on an horizontal curve (solid line) by considering the direction of the tangent vector  $\dot{\gamma}_{2D}(t)$  of the planar curve as the third coordinate. Then, tangent vectors  $\dot{\gamma}(t) \in \text{span}\{\mathcal{A}_1|_{\gamma(t)}, \mathcal{A}_2|_{\gamma(t)}\} = \Delta|_{\gamma(t)}$ , Eq. (1). **B:** In the lifted domain  $SE(2)$  crossing structures are disentangled. **C:** The SR-geodesic (green) better follows the curvilinear structure along the gap than the Riemannian geodesic (red).

new wavefront propagation-based method for finding SR-geodesics within  $SE(2)$  with a metric tensor depending on a smooth external cost  $\mathcal{C} : SE(2) \rightarrow [\delta, 1]$ ,  $\delta > 0$  fixed. Our solution is based on a Hamilton-Jacobi-Bellman (HJB) equation in  $SE(2)$  with a SR metric including the cost. Using Pontryagin’s Maximum Principle (PMP), we derive the HJB-system with an Eikonal equation providing the propagation of geodesically equidistant surfaces departing from the origin. We prove this in Thm. 1, and we show that SR-geodesics are computed by backtracking via PMP. In Thm. 2, we consider the case  $\mathcal{C} = 1$  and we show that the surfaces coincide with the SR-spheres, i.e. the surfaces from which every tracked curve is globally optimal. We find a remarkable accuracy compared to exact solutions, 1st Maxwell sets, and to the cusp surface [7, 14]. Potential towards applications of the method with non-uniform cost is demonstrated by performing vessel tracking in retinal images. Here the cost function is computed by lifting the images via oriented wavelets, as is explained in Section 3.1. Similar ideas of

computing geodesics via wavefront propagation in the extended image domain of positions and orientations, and/or scales, have been proposed in [5, 17, 23]. In addition to these interesting works we propose to rely on a SR geometry. Let us illustrate some key features of our method. In Fig. 1B one can see how disentanglement of intersecting structures, due to their difference in orientations, allows to automatically deal with crossings (a similar result can be obtained with the algorithm in [23]). The extra benefit of using a SR geometry is shown in Fig. 1C where the SR-geodesic better follows the curvilinear structure along the gap.

## 2 Problem Formulation

The roto-translation group  $SE(2)$  is equipped with the group product:  $gg' = (\mathbf{x}, R_\theta)(\mathbf{x}', R_{\theta'}) = (R_\theta\mathbf{x}' + \mathbf{x}, R_{\theta+\theta'})$ , where  $R_\theta$  is a counter-clockwise planar rotation over angle  $\theta$ . This group can be naturally identified with the coupled space of positions and orientations  $\mathbb{R}^2 \times S^1$ , by identifying  $R_\theta \leftrightarrow \theta$  while imposing  $2\pi$ -periodicity on  $\theta$ . Then for each  $g \in SE(2)$  we have the left multiplication  $L_g h = gh$ . Via the push-forward  $(L_g)_*$  of the left-multiplication we get the left-invariant vector fields  $\{\mathcal{A}_1, \mathcal{A}_2, \mathcal{A}_3\}$  from the Lie-algebra basis  $\{\mathcal{A}_1, \mathcal{A}_2, \mathcal{A}_3\} = \{\partial_x|_e, \partial_\theta|_e, \partial_y|_e\}$  at the unity  $e = (0, 0, 0)$ :

$$\begin{aligned} \mathcal{A}_1|_g &= \cos \theta \partial_x|_g + \sin \theta \partial_y|_g = (L_g)_* \partial_x|_e, \\ \mathcal{A}_2|_g &= \partial_\theta|_g = (L_g)_* \partial_\theta|_e, \\ \mathcal{A}_3|_g &= -\sin \theta \partial_x|_g + \cos \theta \partial_y|_g = (L_g)_* \partial_y|_e. \end{aligned} \tag{1}$$

So all tangents  $\dot{\gamma}(t) \in T_{\gamma(t)}(SE(2))$  along smooth curves  $t \mapsto \gamma(t) \in SE(2)$  can be expanded as  $\dot{\gamma}(t) = \sum_{k=1}^3 u^k(t) \mathcal{A}_k|_{\gamma(t)}$ , where the contravariant components  $u^k(t)$  of the tangents (velocities) can be considered as the control variables. Not all curves  $t \mapsto \gamma(t) = (x(t), y(t), \theta(t))$  in  $SE(2)$  are naturally lifted from the plane in the sense that  $\theta(t) = \arg(\dot{x}(t) + i\dot{y}(t))$ . This only holds for so-called *horizontal curves* which have  $u^3 = 0$  and thus  $\dot{\gamma}(t) = \sum_{k=1}^2 u^k(t) \mathcal{A}_k|_{\gamma(t)}$ . The allowed (horizontal) directions in tangent bundle  $T(SE(2))$  form a so-called distribution  $\Delta := \text{span}\{\mathcal{A}_1, \mathcal{A}_2\}$ , see Fig. 1A.

Therefore we consider SR-manifold [21]  $(SE(2), \Delta, G^C)$ , with  $G^C : SE(2) \times \Delta \times \Delta \rightarrow \mathbb{R}$  denoting the inner product given by

$$G^C|_{\gamma(t)}(\dot{\gamma}(t), \dot{\gamma}(t)) = \mathcal{C}^2(\gamma(t)) \left( \beta^2 |\dot{x}(t) \cos \theta(t) + \dot{y}(t) \sin \theta(t)|^2 + |\dot{\theta}(t)|^2 \right), \tag{2}$$

with  $\gamma : \mathbb{R} \rightarrow SE(2)$  a smooth curve on  $\mathbb{R}^2 \times S^1$ ,  $\beta > 0$  constant,  $\mathcal{C} : SE(2) \rightarrow [\delta, 1]$  the *given external smooth cost which is bounded from below by  $\delta > 0$* .

*Remark 1.* Define  $\mathcal{L}_g \phi(h) = \phi(g^{-1}h)$  then we have:

$$G^C|_{\gamma}(\dot{\gamma}, \dot{\gamma}) = G^{\mathcal{L}_g \mathcal{C}}|_{g\gamma} \left( (L_g)_* \dot{\gamma}, (L_g)_* \dot{\gamma} \right).$$

Thus,  $G^C$  is not left-invariant, but if shifting the cost as well, we can, for the computation of SR-geodesics, restrict ourselves to  $\gamma(0) = e$ .

We study the problem of finding SR minimizers, i.e. for given boundary conditions  $\gamma(0) = e, \gamma(T) = g$ , we aim to find a horizontal curve  $\gamma(t)$  (having  $\dot{\gamma} \in \Delta$ ) that minimizes the total SR length

$$l = \int_0^T \sqrt{G^c|_{\gamma(t)}(\dot{\gamma}(t), \dot{\gamma}(t))} dt. \tag{3}$$

If  $t$  is the SR arclength parameter, which will be our default parameter here, then  $\sqrt{G^c|_{\gamma(t)}(\dot{\gamma}(t), \dot{\gamma}(t))} = 1$  and  $l = T$ . Then, SR minimizers are solutions to the optimal control problem (with free  $T > 0$ ):

$$\begin{aligned} \dot{\gamma} &= u^1 \mathcal{A}_1|_{\gamma} + u^2 \mathcal{A}_2|_{\gamma}, \\ \gamma(0) &= e, \quad \gamma(T) = g, \\ l(\gamma(\cdot)) &= \int_0^T \mathcal{C}(\gamma(t)) \sqrt{\beta^2 |u^1(t)|^2 + |u^2(t)|^2} dt \rightarrow \min, \\ \gamma(t) &\in SE(2), \quad (u^1(t), u^2(t)) \in \mathbb{R}^2, \quad \beta > 0. \end{aligned} \tag{4}$$

Stationary curves of this problem are found via PMP [1].

*Remark 2.* The Cauchy-Schwarz inequality implies that the minimization problem for the SR length functional  $l$  is equivalent (see e.g. [21]) to the minimization problem for the action functional with fixed  $T$ :

$$J(\gamma) = \frac{1}{2} \int_0^T \mathcal{C}^2(\gamma(t)) (\beta^2 |u^1(t)|^2 + |u^2(t)|^2) dt. \tag{5}$$

### 3 Solutions via Data-Driven Wavefront Propagation

The following theorem summarizes our method for the computation of data-adaptive sub-Riemannian geodesics in  $SE(2)$ , and is illustrated in Fig. 2.

**Theorem 1.** *Let  $W^\infty(g)$  be a solution of the boundary value problem (BVP) with Eikonal-equation*

$$\begin{cases} 1 - \sqrt{(\mathcal{C}(g))^{-2} (\beta^{-2} |\mathcal{A}_1 W^\infty(g)|^2 + |\mathcal{A}_2 W^\infty(g)|^2)} = 0, \text{ for } g \neq e, \\ W^\infty(e) = 0. \end{cases} \tag{6}$$

*Then the iso-contours*

$$\mathcal{S}_t = \{g \in SE(2) \mid W^\infty(g) = t\} \tag{7}$$

*are geodesically equidistant with speed  $\frac{dt}{dt} = \mathcal{C}(\gamma(t)) \sqrt{\beta^2 |u^1(t)|^2 + |u^2(t)|^2} = 1$  and they provide a specific part of the SR-wavefronts departing from  $e = (0, 0, 0)$ . A SR-geodesic departing from  $g \in SE(2)$  is found by backward integration*

$$\dot{\gamma}_b(t) = -\frac{\mathcal{A}_1 W^\infty|_{\gamma_b(t)}}{(\beta \mathcal{C}(\gamma_b(t)))^2} \mathcal{A}_1|_{\gamma_b(t)} - \frac{\mathcal{A}_2 W^\infty|_{\gamma_b(t)}}{(\mathcal{C}(\gamma_b(t)))^2} \mathcal{A}_2|_{\gamma_b(t)}, \quad \gamma_b(0) = g. \tag{8}$$

As the proof of Thm. 1 is lengthy, we do not include its details in this conference paper. For the proof see [4]. In fact, the results on geodesically equidistant surfaces follow from connecting the Fenchel transform on  $\Delta$ , to the Fenchel transform on  $\mathbb{R}^2$  (Lemma 1 in [4, App. C]). Then, we derive the HJB-equation for the homogeneous Lagrangian as a limit from the HJB-equation for the squared Lagrangian (Lemma 2 in [4, App. C.1]). The back-tracking result follows from applying PMP to (5), (see [4, App. C.1]). Akin to the  $\mathbb{R}^d$ -case [8], characteristics are found by PMP.  $\square$

To obtain an iterative implementation to solve BVP Eq. (6), relying on viscosity solutions of initial value problems (IVP), we resort to subsequent auxiliary IVP's on  $SE(2)$  for each  $r \in [r_0, r_0 + \epsilon]$ , with  $r_0 = n\epsilon$  at step  $n \in \mathbb{N} \cup \{0\}$ ,  $\epsilon > 0$  fixed:

$$\begin{cases} \frac{\partial W^\epsilon}{\partial r}(g, r) = 1 - \sqrt{(\mathcal{C}(g))^{-2} (\beta^{-2} |\mathcal{A}_1 W^\epsilon(g, r)|^2 + |\mathcal{A}_2 W^\epsilon(g, r)|^2)}, \\ W^\epsilon(g, r_0) = W_{r_0}^\epsilon(g). \end{cases} \quad (9)$$

Here  $W_{r_0=0}^\epsilon = \delta_e^M$  is the morphological delta (i.e.  $\delta_e^M(g) = 0$  if  $g = e$ , and  $\delta_e^M(g) = \infty$  if  $g \neq e$ ). After each iteration at time-step  $r = r_0$ , we update  $W^\epsilon(e, r_0) = W_{r_0}^\epsilon(e) = 0$ . For  $g \neq e$  and  $n \geq 1$  we set  $W_{r_0}^\epsilon(g) = W_{r_0-\epsilon}^\epsilon(g, r_0)$  (i.e. we use, only for  $g \neq e$ , the end condition at step  $n$  for the initial condition at step  $n + 1$ ). Then we obtain

$$W^\infty(g) = \lim_{\epsilon \rightarrow 0} \lim_{n \rightarrow \infty} W^\epsilon(g, (n + 1)\epsilon). \quad (10)$$

Here we stress that, by general semigroup theory [2], *one cannot impose both the initial condition and a boundary condition  $W^\epsilon(e, r) = 0$  at the same time*, which forced us to update the initial condition (at  $g = e$ ) in our implementation scheme. It is important for optimality results below, that the solution  $W^\epsilon(g, r)$  obtained from  $W^\epsilon(g, r_0) = W_{r_0}^\epsilon(g)$  is the unique *viscosity* solution of (9).

The next theorem provides our main theoretical result. Recall that Maxwell points are  $SE(2)$  points where two distinct geodesics with the same length meet.

**Theorem 2.** *Let  $\mathcal{C} = 1$ . Let  $W^\infty(g)$  be given by (10), based on viscosity solutions of (9), solving (6). Then  $\mathcal{S}_t$  equals the SR-sphere of radius  $t$ . Backward integration via (8) provides globally optimal geodesics reaching  $e$  at  $t = d(g, e) :=$*

$$\min_{\substack{\gamma \in C^\infty(\mathbb{R}^+, SE(2)), T \geq 0, \\ \dot{\gamma} \in \Delta, \gamma(0) = e, \gamma(T) = g}} \int_0^T \sqrt{|\dot{\theta}(t)|^2 + \beta^2 |\dot{x}(t) \cos \theta(t) + \dot{y}(t) \sin \theta(t)|^2} dt,$$

and  $\gamma_b(t) = \gamma^{min}(d(g, e) - t)$ . The SR-spheres  $\mathcal{S}_t = \{g \in SE(2) \mid d(g, e) = t\}$  are non-smooth at the 1st Maxwell set  $\mathcal{M}$ , cf. [27],

$$\mathcal{M} \subset \left\{ (x, y, \theta) \in SE(2) \mid x \cos \frac{\theta}{2} + y \sin \frac{\theta}{2} = 0 \vee \theta = \pi \right\}, \quad (11)$$

and the back-tracking (8) does not pass the 1st Maxwell set.

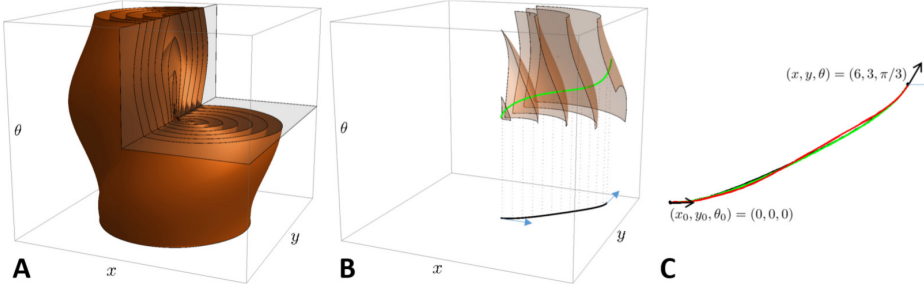


**Fig. 2.** **A-B:** Our method provides both geodesically equidistant surfaces  $\mathcal{S}_t$  (7) and SR-geodesics. Geodesic equidistance holds with unit speed for all SR-geodesics passing through the surface, see Thm 1. Via Thm. 2 we have that  $W^\infty(g) = d(g, e)$  and  $\{\mathcal{S}_t\}_{t \geq 0}$  is the family of SR-spheres with radius  $t$  depicted in this figure. They are non-smooth at the 1st Maxwell set  $\mathcal{M}$ . **C:** SR-geodesic example (for  $C = 1$ ) shows our PDE-discretizations (with 12 and 64 sampled orientations in red and green resp.) are accurate in comparison to analytic approaches (black) in [14, 27].

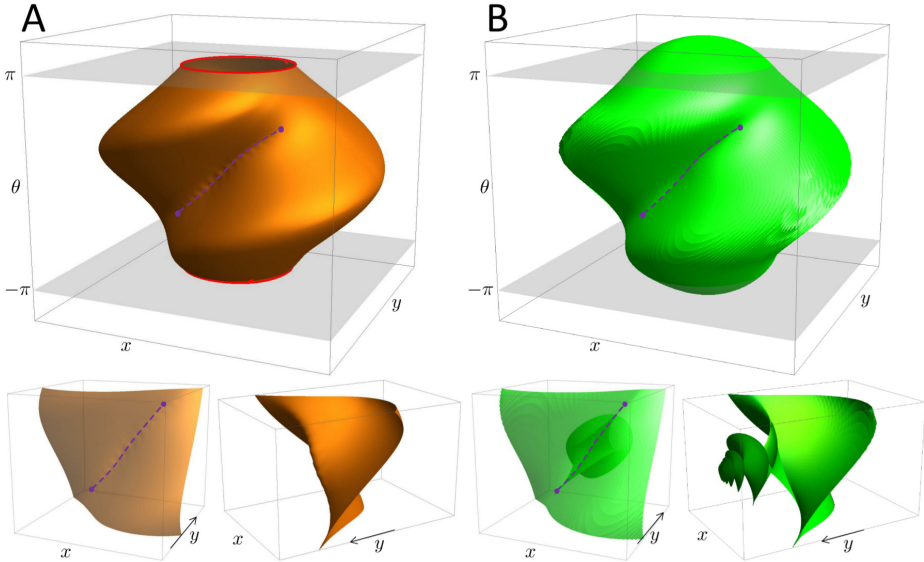


**Fig. 3.** **A:** SR-sphere  $\mathcal{S}_t$  for  $t = 4$  obtained by the method in Thm. 1 using  $C = 1$  and  $\delta_e^M$  as initial condition via viscosity solutions of the HJB-equation (9) implemented according to Section 4. **B:** The full SR-wavefront departing from  $e$  via the method of characteristics giving rise to interior folds (corresponding to multiple valued non-viscosity solutions of the HJB-equation). The Maxwell set  $\mathcal{M}$  consists precisely of the dashed line on  $x \cos \frac{\theta}{2} + y \sin \frac{\theta}{2} = 0$  and the red circles at  $|\theta| = \pi$ . The dots are 2 (of the 4) conjugate points on  $\mathcal{S}_t$  which are limits of 1st Maxwell points (but not Maxwell points themselves). In **B** we see the astroidal structure of the conjugate locus [10, 20]. In **A** we see that the *unique* viscosity solutions stop at the 1st Maxwell set. Comparison of **A** and **B** shows the global optimality and accuracy of our method at **A**.

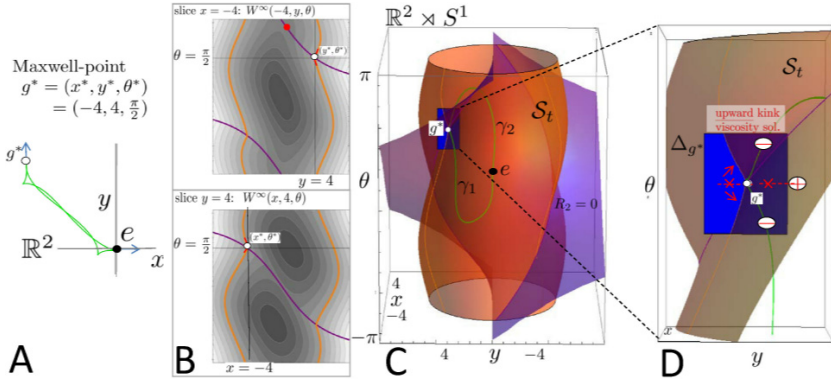


**Fig. 4.** Maxwell point  $g^* = (-4, 4, \pi/2)$  (in white) on SR-sphere  $S_t$  (in orange) for  $C = 1$ . At  $g^*$  two SR-geodesics  $\gamma_1 \neq \gamma_2$  with equal SR-length  $t$  meet ( $\gamma_1(t) = \gamma_2(t)$ ). From left to right: **A:** projection of  $\gamma_1$  and  $\gamma_2$  on the plane  $(x, y)$ , **B:** 2D-slices ( $x = x^*$ ,  $y = y^*$ ) of level sets of  $W^\infty(g)$  with distinguished value  $W^\infty(g) = t$  (again in orange). On top we plotted, the Maxwell point, the intersection of surface  $x \cos \frac{\theta}{2} + y \sin \frac{\theta}{2} = 0$  (in purple, this set contains a part of the 1st Maxwell set) with the 2D-slices. **C:** The SR-sphere  $S_t$  in  $SE(2)$ , **D:** section around  $g^*$  revealing the upward kink due to the viscosity solution. From this kink we see that the tracking (8) does not cross a 1st Maxwell point as indicated in red, yielding global optimality in Thm. 2.

Proof of Thm. 2 can be found in [4, App. C.2]. The global optimality and the non-passing of the 1st Maxwell set can be observed in Fig. 3. The geometrical idea of the proof is illustrated in Fig. 4.

*Remark 3.* The stationary solutions of (9) satisfy the SR-Eikonal equation (6). The Hamiltonian  $H^{fixed}$  for the equivalent fixed time problem (5) equals  $H^{fixed}(g, p) = (C(g))^{-2} (\beta^{-2} h_1^2 + h_2^2) = 1/2$ , with momentum covector  $p = h_1 \omega^1 + h_2 \omega^2 + h_3 \omega^3$  expressed in dual basis  $\{\omega^i\}_{i=1}^3$  given by  $\langle \omega^i, \mathcal{A}_j \rangle = \delta_j^i$ . The Hamiltonian  $H^{free}$  for the free time problem (4) minimizing  $l$  equals  $H^{free}(g, p) = \sqrt{2H^{fixed}(g, p)} - 1 = 0$ . For details see [4, App. A and C]. Eq. (6) can be written as  $H^{free}(g, p) = 0$  with momentum covector equal to  $p = \sum_{i=1}^2 (\mathcal{A}_i W^\infty) \omega^i$ .

*Remark 4.* SR geodesics loose their optimality either at a Maxwell point or at a conjugate point (where the integrator of the canonical ODE's, mapping initial momentum  $p_0$  and time  $t > 0$  to end-point  $\gamma(t)$ , is degenerate [1]). Some conjugate points are limits of Maxwell points, see Fig. 4, where the 1st astroidal shaped conjugate locus coincides with the void regions (cf. [3, fig.1]) after 1st Maxwell set  $\mathcal{M}$ . When setting a Maxwell point as initial condition, initial gradient  $dW|_{\gamma_b(0)}$  is not defined. Here there are 2 horizontal directions with minimal slope, taking these directions our algorithm produces the result in Fig. 6B.

*Remark 5.* The choice of our initial condition comes from the relation between linear and morphological scale spaces [2, 9]. Here, for linear  $SE(2)$ -convolutions

over the  $(\cdot, +)$ -algebra one has  $\delta_e *_{SE(2)} U = U$ . For morphological  $SE(2)$ -convolutions over the  $(\min, +)$ -algebra [14] one has a similar property:

$$(\delta_e^M \ominus U)(g) := \inf_{q \in SE(2)} \{ \delta_e^M(q^{-1}g) + U(q) \} = U(g), \tag{12}$$

This is important for representing viscosity solutions of left-invariant HJB-equations on  $SE(2)$  by Lax-Oleinik [15] type of formulas (akin to the  $SE(3)$ -case [13]).

### 3.1 Construction of the Non-uniform Cost

The cost should have low values on locations with high curve saliency, and high values otherwise. Based on image  $f$  we define the cost-function  $\delta \leq C \leq 1$  via

$$C(\mathbf{x}, \theta) = \delta + (1 - \delta)e^{-\lambda \mathcal{V}(\mathbf{x}, \theta)}, \quad \lambda > 0, \tag{13}$$

with  $\mathcal{V}(\mathbf{x}, \theta) = \left| \frac{\mathcal{W}_\psi f(\mathbf{x}, \theta)}{\|\mathcal{W}_\psi f\|_\infty} \right|^p$ ,  $p > 1$ , a differentiable function in which the lines are enhanced, and where the lifting is done using anisotropic wavelets  $\psi$ :

$$(\mathcal{W}_\psi f)(\mathbf{x}, \theta) = \int_{\mathbb{R}^2} \overline{\psi(R_\theta^{-1}(\mathbf{y} - \mathbf{x}))} f(\mathbf{y}) d\mathbf{y}. \tag{14}$$

Here we take the modulus of the image lifted by (quadrature) wavelets  $\psi$  as a basic technique for the detection of curvi-linear structure. The power with exponent  $p$  after a max-normalization to  $[0, 1]$  is used to sharpen the data. In this work we use so-called cake wavelets [12] to do the lifting. These wavelets have the property that they allow stable reconstruction and do not tamper data evidence before processing takes place in the  $SE(2)$  domain. Other type of 2D wavelets could be used as well. In related work by Péchaud et al. [23] the cost  $C$  was obtained via normalized cross correlation with a set of templates. In Eq. (13) two parameters,  $\delta$  and  $\lambda$ , are introduced. Parameter  $\delta$  is used as a lower bound on the cost function, and may be used to increase the contrast in the cost function. E.g., by choosing  $\delta = 1$  one creates a uniform cost function and by choosing  $\delta < 1$  one adds more contrast. Parameter  $\lambda$  is used as a soft-thresholding parameter.

## 4 Implementation

To compute the SR geodesics with given boundary conditions we first construct the value function  $W^\infty$  in Eq. (6), implementing the iterations at Eq. (9), after which we obtain our geodesic  $\gamma$  via a gradient descent on  $W^\infty$  from  $g$  back to  $e$ , recall Thm. 1 (and Thm. 2). We use an iterative upwind scheme to obtain the viscosity solution  $W^\epsilon$  at iteration Eq. (9). Here we initialize  $W^\epsilon(\cdot, 0) = \delta_e^{MD}(\cdot)$ , with the discrete morphological delta, given by  $\delta^{MD}(g) = 0$  if  $g = e$  and 1 if  $g \neq e$ , and iterate

$$\begin{cases} W^\epsilon(g, r + \Delta r) = W^\epsilon(g, r) - \Delta r H_D^{free}(g, dW^\epsilon(g, r)) & \text{for } g \neq e \\ W^\epsilon(e, r + \Delta r) = 0, \end{cases} \tag{15}$$

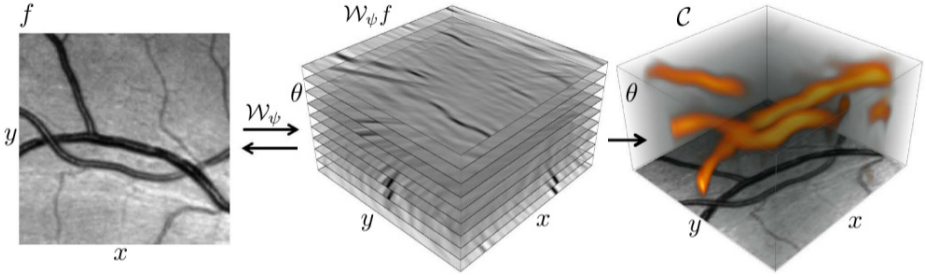


**Fig. 5.** Left: retinal image  $f$  and corresponding function  $\mathcal{W}_\psi f$  (‘invertible orientation score’) using a cake-wavelet  $\psi$  [12]. The cost  $\mathcal{C}$ , constructed via the modulus of the score cf. (13) with  $p = 3$ ,  $\delta = 0.3$ ,  $\lambda = 30$ , yields a differentiable function.

with  $H_D^{free}(g, dW^\epsilon(g, r)) = \left( \frac{1}{c(g)} \sqrt{\beta^{-2}(\mathcal{A}_1 W^\epsilon(g, r))^2 + (\mathcal{A}_2 W^\epsilon(g, r))^2} - 1 \right)$  until convergence. We set  $\Delta r = \epsilon$  in Eq. (9). In the numerical upwind scheme we set  $(\mathcal{A}_i W^\epsilon(g, r))^2 = (\max\{\mathcal{A}_i^- W^\epsilon(g, r), -\mathcal{A}_i^+ W^\epsilon(g, r), 0\})^2$ , where  $\mathcal{A}_i^+$  and  $\mathcal{A}_i^-$  denote respectively the forward and backward finite difference approximations of  $\mathcal{A}_i$ . Here finite differences applied in the moving frame, using  $B$ -spline interpolation, are favorable over finite differences in the fixed coordinate grid  $\{x, y, \theta\}$ . For details on left-invariant finite differences and comparisons see [16]. In our implementation the origin  $e$  is treated separately as our initial condition is not differentiable. We apply the update  $W^\epsilon(e, r) = 0$  for all  $r \in \epsilon\mathbb{N}$ . We set step size  $\epsilon = 0.1 \min(s_{xy}\beta, s_\theta)$  with  $s_{xy}$  and  $s_\theta$  step sizes in respectively the  $x$ - $y$ -directions and  $\theta$ -direction.

## 5 Experiments and Results

### 5.1 Comparison and Validation $\mathcal{C} = 1$ Case

Throughout the paper we have illustrated the theory with figures obtained via our new wavefront propagation technique. In this section we go through the figures that support the accuracy of our method. As the problem (4) for  $\mathcal{C} = 1$  was solved [14,27], we use this as a basis for comparison. Unless indicated otherwise, we used the implementation details as described in Section 4, and worked with a  $\{x, y, \theta\}$ -121 × 121 × 64 grid.

Let us consider Fig. 2C. Here an arbitrary SR-geodesic between the SE(2) points  $\gamma(0) = e$  and  $\gamma(T) = (6, 3, \pi/3)$  is found via the initial value problem in [27] with end-time  $T = 7.11$  and initial momentum  $p_0 = h_1(0)dx + h_2(0)dy + h_3(0)d\theta$ , with  $h_1(0) = \sqrt{1 - |h_2(0)|^2}$ ,  $h_2(0) = 0.430$  and  $h_3(0) = -0.428$ , is used for reference (black curve in Fig 2C). Using the semi-analytic approach in [14] an almost identical result is obtained. The curves computed with our method with angular step-sizes of  $2\pi/12$  and  $2\pi/64$  are shown in Fig 2C in red and green respectively. Already at low resolution we observe accurate results.

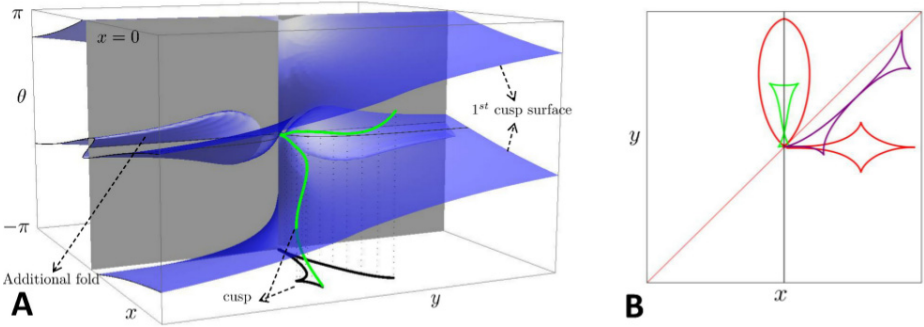


**Fig. 6. A:** The blue surface represents the cusp surface numerically computed via the proposed HJB-system (with  $C = 1$ ) and subsequent calculation of the zero-crossings of  $\mathcal{A}_1 W^\infty(x, y, \theta)$ . Indeed if a SR-geodesic (in green) passes this surface, it passes in  $\theta$ -direction (with infinite curvature [7, 14]), yielding a cusp on the spatial ground plane. The same blue surface is computed in [14, Fig. 11]. We even see the additional fold (top left passing the grey-plane) as some globally optimal SR-geodesics even exhibit 2 cusps. **B:** Different configurations of projected SR-geodesics ending in Maxwell points, computed with our method.

In Fig. 3 we compare one SR-sphere for  $T = 4$  (Fig. 3A) found via our method with the full SR-wavefront departing from  $e$  (Fig. 3B) computed by the method of characteristics [27]. We observe that our solution is non-smooth at the 1st Maxwell set  $\mathcal{M}$  (11) and that the unique viscosity solution stops precisely there. Finally, the blue surface in Fig. 6A represents the cusp surface, i.e. the surface consisting of all cusp points. Cusps are singularities that can occur on geodesics when they are projected into the image plane (see Fig. 6A). This happens at points  $g_c$  where the geodesic is tangent to the vector  $\partial_\theta|_{g_c} = \mathcal{A}_2|_{g_c}$  and this implies that the control  $u_1$  vanishes. Then, the cusp surface is easily computed as the zero-crossing of  $\mathcal{A}_1 W^\infty(x, y, \theta)$ . The obtained surface is in agreement with the exact cusp surface given in [14, Fig. 11].

**5.2 Feasibility Study for Application in Retinal Imaging**

As a feasibility study for the application of our method in retinal images we tested the method on three image patches exhibiting both crossings and bifurcations (Fig. 7). For each patch two seed points were selected manually, one for an artery (red) and one for a vein (blue). For each seed point the value function  $W$  was calculated according to the implementation details in Section 4, after which multiple end-points were traced back to the seed point. The image dimensions were respectively  $200 \times 200$ ,  $125 \times 125$  and  $125 \times 125$ . For the construction of the cost function we set  $p = 3$ ,  $\delta = 0.3$ ,  $\beta = 0.1$ ,  $\lambda = 30$  (see e.g. Fig. 5), and the lifting was done using cake wavelets with angular resolution  $2\pi/32$ .

In Fig. 7 we see that all selected end-points were traced back correctly, and that the tracks smoothly follow the actual vessels. We note here that our

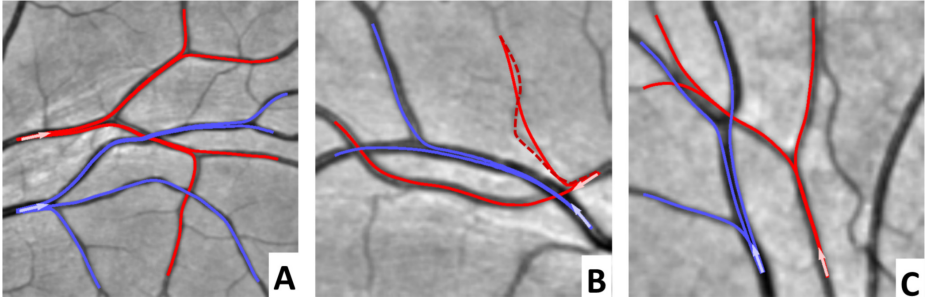


**Fig. 7.** Data-adaptive sub-Riemannian geodesics obtained via our proposed tracking method (Thm. 2), with external cost (13), with  $p = 3$ ,  $\delta = 0.3$ ,  $\beta = 0.1$ ,  $\lambda = 30$ . The dashed, dark-red, curve indicates results obtained with  $\beta = .5$ .

sub-Riemannian approach enforces smoothness, and that flexibility is controlled via parameter  $\beta$ . This is a convenient property as it increases robustness to noise, missing data and complex crossing structures. However, it might not be wise to set the  $\beta$  parameter globally, as we did in these experiments, since smaller vessels are typically more tortuous and therefore require more flexibility. To demonstrate the effect of a larger value for  $\beta$  we retraced the small and low-contrast blood vessel in Fig. 7B (see dashed dark-red curve) with  $\beta = .5$  and see that it now more accurately follows the true vessel curve. In this study, we do not focus on the precise centerline extraction, this could however be achieved by considering the vessel width as an extra feature (as in [5, 17, 23]).

## 6 Conclusion

In this paper we propose a novel, flexible and accurate numerical method for computing solutions to the optimal control problem (4), i.e. finding SR-geodesics in  $SE(2)$  with non-uniform cost. The method consists of a wavefront propagation of geodesically equidistant surfaces computed via the viscosity solution of a HJB-system in  $(SE(2), \Delta, G^C)$ , and subsequent backwards integration, which gives the optimal tracks. We used PMP to derive both the HJB-equation and the backtracking. We have shown global optimality for the uniform case ( $C=1$ ) and that our method generates geodesically equidistant surfaces. Compared to previous works regarding SR-geodesics in  $(SE(2), \Delta, G^1)$  [14, 18, 27], we solve the boundary value problem without shooting techniques, using a computational method that always provides the optimal solution. Compared with wavefront propagation methods on the extended domain of positions and orientations in image analysis [23, 24], we consider a sub-Riemannian metric instead of a Riemannian metric. Results in retinal vessel tracking are promising.

Fast, efficient implementation using ordered upwind schemes (such as the anisotropic Fast Marching method presented in [19]) is planned as future work as well as adaptation to other Lie groups such as  $SE(3)$  and  $SO(3)$ . Of particular interest in neuroimaging is application to high angular resolution diffusion imaging (HARDI) by considering the extension to  $SE(3)$  [13,24].

## References

1. Agrachev, A.A., Sachkov, Y.L.: Control Theory from the Geometric Viewpoint. Springer, Heidelberg (2004)
2. Akian, M., Quadrat, J.P., Viot, M.: Bellman processes. In: 11th Int. Conf. on Analysis and Opt. Systems. LNCIS. Springer-Verlag (1994)
3. Bayen, A.M., Tomlin, C.J.: A construction procedure using characteristics for viscosity solutions of the Hamilton-Jacobi equation. In: 40th IEEE Conf. on Decision and Control, pp. 1657–1662 (2001)
4. Bekkers, E., Duits, R., Mashtakov, A., Sanguinetti, G.: A PDE approach to Data-Driven Sub-Riemannian Geodesics. Preprint on arxiv (2015)
5. Benmansour, F., Cohen, L.D.: Tubular Structure Segmentation Based on Minimal Path Method and Anisotropic Enhancement. IJCV **92**(2), 192–210 (2011)
6. Ben-Yosef, G., Ben-Shahar, O.: A tangent bundle theory for visual curve completion. PAMI **34**(7), 1263–1280 (2012)
7. Boscain, U., Duits, R., Rossi, F., Sachkov, Y.: Curve Cuspless reconstruction via sub-Riemannian geometry. ESAIM: COCV **20**, pp. 748–770 (2014)
8. Bressan, A.: Viscosity Solutions of Hamilton-Jacobi Equations and Optimal Control Problems. Pennsylvania State University, Lecture Notes Dep. of Math. (2011)
9. Burgeth, B., Weickert, J.: An Explanation for the Logarithmic Connection between Linear and Morphological System Theory. IJCV **64**(2–3), 157–169 (2005)
10. Chakir, H., Gauthier, J.P., Kupka, I.: Small Subriemannian Balls on  $\mathbb{R}^3$ . JDCS **2**(3), 359–421 (1996)
11. Citti, G., Sarti, A.: A Cortical Based Model of Perceptual Completion in the Roto-Translation Space. JMIV **24**(3), 307–326 (2006)
12. Duits, R., Felsberg, M., Granlund, G., Romeny, B.H.: Image Analysis and Reconstruction using a Wavelet Transform Constructed from a Reducible Representation of the Euclidean Motion Group. IJCV **72**(1), 79–102 (2007)
13. Duits, R., Haije, T.D., Creusen, E., Ghosh, A.: Morphological and Linear Scale Spaces for Fiber Enhancement in DW-MRI. JMIV **46**(3), 326–368 (2013)
14. Duits, R., Boscain, U., Rossi, F., Sachkov, Y.: Association Fields via Cuspless Sub-Riemannian Geodesics in  $SE(2)$ . JMIV **49**(2), 384–417 (2014)
15. Evans, L.C.: Partial Differential Equations. Graduate Studies in Mathematics, vol. 19. AMS, Providence (USA) (1998)
16. Franken, E., Duits, R.: Crossing-Preserving Coherence-Enhancing Diffusion on Invertible Orientation Scores. IJCV **85**(3), 253–278 (2009)
17. Li, H., Yezzi, A.: Vessels as 4-d curves: Global minimal 4-d paths to extract 3-d tubular surfaces and centerlines. IEEE TMI **26**, 1213–1223 (2007)
18. Mashtakov, A.P., Ardentov, A.A., Sachkov, Y.L.: Parallel algorithm and software for image inpainting via sub-Riemannian minimizers on the group of rototranslations. Numer. Methods, Theory Appl. **6**(1), 95115 (2013)
19. Mirebeau, J.-M.: Anisotropic Fast-Marching on cartesian grids using Lattice Basis Reduction. SIAM J. Num. Anal. **52**(4), 1573 (2014)

20. Moiseev, I., Sachkov, Y.L.: Maxwell strata in sub-Riemannian problem on the group of motions of a plane. *ESAIM: COCV* 16, no. 2, pp. 380–399 (2010)
21. Montgomery, R.: *A Tour of Subriemannian Geometries*. American Mathematical Society, Their Geodesics and Applications (2002)
22. Osher, S., Fedkiw, R.P.: *Level set methods and dynamic implicit surfaces*. Applied mathematical science. Springer, New York (2003)
23. Péchaud, M., Peyré, G., Keriven, R.: Extraction of Tubular Structures over an Orientation Domain. In: *Proc. IEEE Conf. CVPR*, pp. 336–343 (2009)
24. Péchaud, M., Descoteaux, M., Keriven, R.: Brain connectivity using geodesics in HARDI. In: Yang, G.Z., Hawkes, D., Rueckert, D., Noble, A., Taylor, C. (eds.) *Medical Image Computing and Computer-Assisted Intervention - MICCAI 2009*. LNCS, vol. 5762, pp. 482–489. Springer, Heidelberg (2009)
25. Petitot, J.: The neurogeometry of pinwheels as a sub-Riemannian contact structure. *J. Physiol., Paris* 97, 265–309 (2003)
26. Peyré, G., Péchaud, M., Keriven, R., Cohen, L.D.: Geodesic methods in computer vision and graphics. *Found Trends Comp in Computer Graphics and Vision* 5(34), 197–397 (2010)
27. Sachkov, Y.L.: Conjugate and cut time in the sub-Riemannian problem on the group of motions of a plane. *ESAIM: COCV* 16(4), 1018–1039 (2009)
28. Sethian, J.A.: *Level Set Methods and Fast Marching Methods*. Cambridge University Press (1999)